

Measurement and verification of concentration-dependent diffusion coefficient: Ray tracing imagery of diffusion process

Li Wei(魏利), Wei-Dong Meng(孟伟东), Li-Cun Sun(孙丽存), Xin-Fei Cao(曹新飞), Xiao-Yun Pu(普小云)
Citation: Chin. Phys. B . 2020, 29(8): 084206 . **doi:** 10.1088/1674-1056/ab9435
Journal homepage: http://cpb.iphy.ac.cn; http://iopscience.iop.org/cpb

What follows is a list of articles you may be interested in

Microwave frequency transfer over a 112-km urban fiber link based on electronic phase compensation

Wen-Xiang Xue(薛文祥), Wen-Yu Zhao(赵文宇), Hong-Lei Quan(全洪雷), Cui-Chen Zhao(赵粹臣), Yan Xing(邢燕), Hai-Feng Jiang(姜海峰), Shou-Gang Zhang(张首刚)
Chin. Phys. B . 2020, 29(6): 064209 . **doi:** 10.1088/1674-1056/ab84d6

Spectral distortion of dual-comb spectrometry due to repetition rate fluctuation

Hong-Lei Yang(杨宏雷), Hao-Yun Wei(尉昊赟), Yan Li(李岩)
Chin. Phys. B . 2016, 25(4): 044207 . **doi:** 10.1088/1674-1056/25/4/044207

Joint transfer of time and frequency signals and multi-point synchronization via fiber network

Nan Cheng(程楠), Wei Chen(陈炜), Qin Liu(刘琴), Dan Xu(徐丹), Fei Yang(杨飞), You-Zhen Gui(桂有珍), Hai-Wen Cai(蔡海文)
Chin. Phys. B . 2016, 25(1): 014206 . **doi:** 10.1088/1674-1056/25/1/014206

Optical coherence transfer over 50-km spooled fiber with frequency instability of 2×10^{-17} at 1 s

Ma Chao-Qun, Wu Li-Fei, Jiang Yan-Yi, Yu Hong-Fu, Bi Zhi-Yi, Ma Long-Sheng
Chin. Phys. B . 2015, 24(8): 084209 . **doi:** 10.1088/1674-1056/24/8/084209

Non-contact angle measurement based on parallel multiplex laser feedback interferometry

Zhang Song, Tan Yi-Dong, Zhang Shu-Lian
Chin. Phys. B . 2014, 23(11): 114202 . **doi:** 10.1088/1674-1056/23/11/114202

Measurement and verification of concentration-dependent diffusion coefficient: Ray tracing imagery of diffusion process*

Li Wei(魏利)[1], Wei-Dong Meng(孟伟东)[1,2], Li-Cun Sun(孙丽存)[3], Xin-Fei Cao(曹新飞)[1], and Xiao-Yun Pu(普小云)[1,2,†]

[1] *Department of Physics, Yunnan University, Kunming* 650091, *China*
[2] *Key Laboratory of Quantum Information of Yunnan Province, Yunnan University, Kunming* 650091, *China*
[3] *Department of Physics, Yunnan Normal University, Kunming* 650504, *China*

(Received 25 February 2020; revised manuscript received 20 April 2020; accepted manuscript online 19 May 2020)

Ray tracing method is used to study the propagation of collimated beams in a liquid–core cylindrical lens (LCL), which has dual functions of diffusion cell and image formation. The diffusion images on the focal plane of the used LCL are simulated by establishing and solving both linear and nonlinear ray equations, the calculated results indicate that the complex imaging results of LCL in inhomogeneous media can be treated by the law of ray propagation in homogeneous media under the condition of small refractive index gradient of diffusion solution. Guided by the calculation conditions, the diffusion process of triethylene glycol aqueous solution is experimentally studied at room temperature by using the LCL in this paper. The spatial and temporal concentration profile $C^{\mathrm{e}}(z,t)$ of diffusion solution is obtained by analyzing diffusion image appearing on the focal plane of the LCL; Then, the concentration-dependent diffusion coefficient is assumed to be a polynomial $D(C) = D_0 \times (1 + \alpha_1 C + \alpha_2 C^2 + \alpha_3 C^3 + \cdots)$. The finite difference method is used to solve the Fick diffusion equation for calculating numerically the concentration profiles $C^n(z,t)$. The $D(C)$ of triethylene glycol aqueous solution is obtained by comparing the $C^n(z,t)$ with $C^{\mathrm{e}}(z,t)$. Finally, the obtained polynomial $D(C)$ is used to calculate the refractive index profiles $n^n(z,t)$s of diffusion solution in the used LCL. Based on the ray propagation law in inhomogeneous media and the calculated $n(z,t)$, the ray tracing method is used again to simulate the dynamic images of the whole experimental diffusion process to varify the correctness of the calculated $D(C)$. The method presented in this work opens up a new way for both measuring and verifying the concentration-dependent liquid diffusion coefficients.

Keywords: concentration-dependent liquid diffusion coefficients, liquid–core cylindrical lens, nonlinear ray equation, ray tracing method

PACS: 42.62.Eh, 07.60.–j, 42.25.Dd, 42.15.Dp **DOI:** 10.1088/1674-1056/ab9435

1. Introduction

Liquid–core cylindrical lens (LCL) is composed of two different cylindrical lenses stuck together as shown in Figs. 1(a) and 1(b), if two kinds of liquids with different refractive indexes (RIs) are injected into the liquid–core successively, the LCL will have the function of diffusion cell. When the collimated beams enter into the LCL along the path perpendicular to the axis of the lens, the image width at different heights has one-to-one sensitive dependence on the RI of the liquid at the corresponding height of the liquid core.[1,2] The spatial RI resolution property of the LCL can be applied to the study of the liquid diffusion process,[3,4] the liquid hygroscopic process,[5] and the solid dissolution in a liquid.[6] Diffusion coefficient is an important datum for studying liquid mass transfer, and its accurate measurement is of important scientific significance and application value for chemical engineering, biology, medicine, environmental protection, and other scientific fields.[7,8] Diffusion coefficient is generally concentration-dependent. The traditional methods of measuring concentration-dependent diffusion coefficient require many diffusion experiments with different concentrations, which are time-consuming and tedious.[9,10] In order to break these limitations, based on an LCL, a novel optical method of measuring rapidly and verifying reliably concentration-dependent liquid diffusion coefficient is demonstrated in this work. However, there are two challenges to be solved in measuring liquid diffusion coefficient by using the LCL. First, due to the diffusion process, the spatial profile of RI in the liquid core is not homogeneous and the ray's propagation in the inhomogeneous medium does not follow the linear propagation property.[11,12] Therefore, it is necessary to study the ray's propagation and imaging law in the LCL composed of inhomogeneous media. Second, the liquid diffusion coefficient is dependent on the concentration in general, so that the diffusion equation has no analytic solution.[13] The second problem to be solved in the work is how to use numerical calculation method to solve the diffusion equation, and obtain the

*Project supported by the National Natural Science Foundation of China (Grant No. 11804296), the Joint Key Project of Yunnan Province, China (Grant Nos. 2018FY001-020 and 2018ZI002), and the Fund from the Educational Department of Yunnan Province, China (Grant No. 2016CYH05).

†Corresponding author. E-mail: xypu@163.com

© 2020 Chinese Physical Society and IOP Publishing Ltd

concentration-dependent diffusion coefficient $D(C)$ by comparing the calculated concentration profiles with experimental diffusion images.

In order to solve the first problem, the spatial and temporal RI profile $n^{s}(z,t)$ of the diffusion solution is obtained by means of a special solution of the diffusion equation, *i.e.*, an analytic solution as the diffusion coefficient is independent of concentration,[1,13] together with the experimental relationship between solution concentration and its RI. Then, a nonlinear ray equation, which is a 2nd-order differential equation of ray propagation in inhomogeneous media, is established and solved numerically in liquid–core region[14,15] Furthermore, when collimated beams pass through either the homogeneous (satisfying linear ray equation) or inhomogeneous solution (satisfying nonlinear ray equation),[17–19] the ray tracing method is used to simulate the diffusion images on the focal plane of the LCL. The computational results of two kinds of diffusion images show that the imaging process in inhomogeneous solution can be treated approximately by the law of ray propagation in homogeneous solution, under the condition of small refractive index gradient of diffusion solution. Taking for example the diffusion process of triethylene glycol (TG) aqueous solution at room temperature (298 K), the conditions of small refractive index gradient are that the difference in initial concentration between two diffusion solutions is less than 60% and the diffusion time is greater than 270 min.

In order to solve the second problem, the experimental diffusion processes of TG aqueous solution under the initial concentration differences of 0%–60% and 40%–100% are studied in the LCL, and the corresponding experimental concentration spatial and temporal profiles $C^{e}(z,\ t)$ of the diffusion solution are obtained during the diffusion time from 270 min to 540 min. Theoretically, the concentration-dependent diffusion coefficient is assumed to satisfy the polynomial expansion relation $D(C) = D_0 \times (1 + \alpha_1 C + \alpha_2 C^2 + \alpha_3 C^3 + \cdots)$, where D is the diffusion coefficient in an infinite dilute solution which can be obtained by analyzing diffusion images in the range of lower concentration; α_1, α_2, and α_3 are under-determined parameters. Then, the finite difference method (FDM) is used to solve numerically the Fick diffusion equation under the initial and boundary conditions the same as the experimental conditions,[20,21] the calculated concentration profiles ($C^{n}(z,t)$) by varying the under-determined parameters are compared with the profile $C^{e}(z,t)$, the parameters (α_1, α_2, α_3, ...) corresponding to the minimum concentration standard deviation between $C^{n}(z,t)$s and $C^{e}(z,t)$ are selected to determine $D(C)$.

To verify the correctness of the obtained $D(C)$, on the one hand, the $D(C)$ is compared with the literature values measured by interferometry at the same temperature.[22,23] On the other hand, the obtained $D(C)$ is substituted into the diffusion equation, the numerical solutions of spatial and temporal RI profiles $n^{n}(z_j,t_i)$ are calculated by means of the FDM. Based on the ray propagation law in inhomogeneous media, the ray tracing method is again used to calculate the dynamic images of whole experimental diffusion process (from 25 min to 540 min). The simulated results are in good agreement with the experimental images in image contour, focal position, and light intensity distribution, which verifies not only the correctness of $D(C)$ measurement results, but also the reliability of treatment on ray propagation in the LCL composed of inhomogeneous diffusion solution in this work.

2. Analysis of image process

If two kinds of liquids with different values of RI of n_4 and n_1 ($n_4 > n_1$, the height of each liquid column is H) are injected into the liquid core successively, and a complementary metal–oxide–semiconductor (CMOS) detector is placed at the position where the RI ($n_c = n_1$) of upper liquid can be sharply imaged, thus, the liquid below presents a diffuse image as shown in Fig. 1(a). As the two liquids diffuse to each other, the solution forms a dynamic RI gradient distribution ($n_4 > n_3 > n_c > n_2 > n_1$) along the diffusion direction (z axis). If the detector is at the focal position of the LCL ($f = f_c$, $n = n_c$), according to the linear propagation law of ray in homogeneous media, the collimated beams entering into the LCL on the xy plane keep propagating in the same plane as shown by the dotted line in Fig. 1(b). The diffusion image is sharply imaged at the position $z = z_c$, while the detector presents a "beam waist" shaped dispersion image at other locations of $z \neq z_c$. As shown on the right of Fig. 1(b), its image width (W_j) at the height of z_j has a one-to-one sensitive dependence on the RI ($n = n_j$) of the solution at the corresponding height z_j, which can be uniquely determined by the geometric relation and imaging law shown in Fig. 1(c), or accurately determined by experimental method.[24]

However, according to the ray propagation law in inhomogeneous media, collimated beams passing through the liquid core will deviate from the entrance plane (xy plane) and propagate as shown by the solid line in Fig. 1(b) due to the fact that the RI of diffusion solution in liquid core is inhomogeneous along the z axis. Can the imaging law in homogeneous media be used to treat approximately the imaging process in inhomogeneous media, and can the light beam deviation from entrance plane be ignored, under the condition that the spatial and temporal RI profile of diffusion solution $n(z,t)$ is undetermined? This is what needs to be analyzed next.

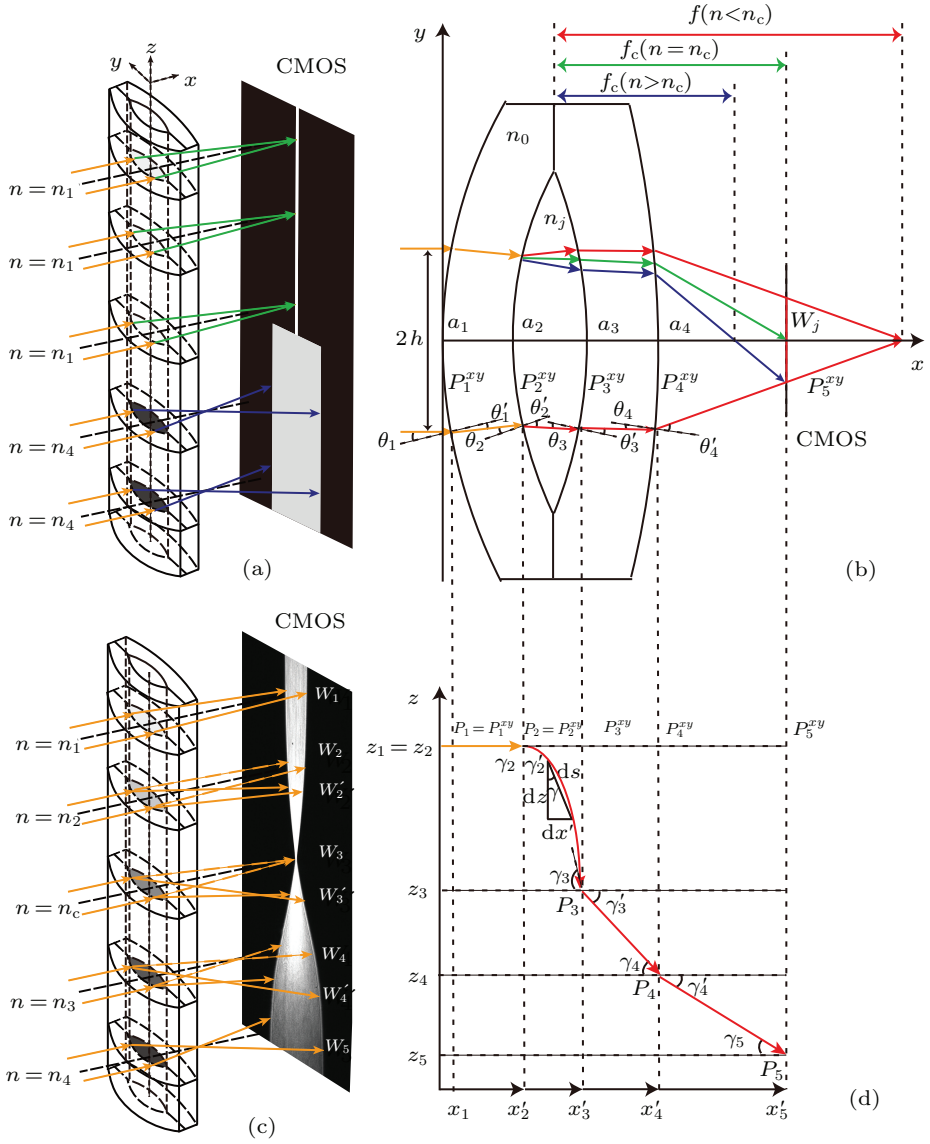


Fig. 1. (a) Three-dimensional (3D) imaging diagram of ray in homogeneous media, (b) 3D imaging diagram of ray in inhomogeneous media, (c) two-dimensional (2D) imaging diagram of ray in homogeneous media (xy plane), and (d) 2D imaging diagram of ray in inhomogeneous media ($x'z$ plane).

3. Ray tracing algorithm in LCL

Based on the Snell law, the ray tracing method is used to track the position of each collimated ray after passing through the LCL and then hitting on a virtual CMOS detector. Light intensity profile is obtained by counting up the ray numbers reaching each pixel of the detector. As shown in Fig. 1(c), the vertices of the four spherical surfaces of the LCL intersect the x axis at a_1, a_2, a_3, and a_4, and their curvature radii are R_1, R_2, R_3, and R_4, respectively. The lens material is K9 glass ($n = 1.5163$). Taking for example one ray incident at point $P_1(x_1, y_1, z_1)$, its ray equations in different light paths are established in the following.

3.1. Linear path of P_1P_2

After entering into the LCL through the 1st spherical surface along the xy plane, the ray keeps propagating on the xy plane (homogeneous media, $n = n_0$) as shown in Figs. 1(c) and 1(d). The coordinates of P_1 $(x_1, y_1, z_1) = P_1^{xy}$ can be calculated by the spherical surface equation $(x - a_1 - R_1)^2 + y^2 = R_1^2$ and the ray equation of the incident ray $y = -h$. The slope of the normal line at P_1 is $k_1' = y_1/(x_1 - a_1 - R_1)$, the incident and refractive angles on the 1st spherical surface are $\theta_1 = \arcsin(h/R_1)$ and $\theta_1' = \arcsin(\sin\theta_1/n_0)$, respectively. The refractive ray intersects with the 2nd spherical surface at P_2 $(x_2, y_2, z_2 = z_1) = P_2^{xy}$, and its slope is $k_1 = \left|\frac{k_1' - \tan\theta_1'}{k_1'\tan\theta_1' + 1}\right|$. Therefore, the coordinates of P_2 can be calculated by the linear ray equation $y = k_1(x - x_1) + y_1$ and the 2nd spherical surface equation $(x - a_2 - R_2)^2 + y^2 = R_2^2$.

3.2. Nonlinear path of P_2P_3

Due to an RI inhomogeneous distribution along the z axis in the liquid core, when the ray P_1P_2 enters into the liquid core through the 2nd spherical surface, refractive ray P_2P_3 will de-

viate from the xy plane propagate on the $\overline{P_2^{xy}P_3^{xy}}z$ plane (inhomogeneous media), and intersects with the 3rd spherical surface at P_3, as shown in Figs. 1(c) and 1(d).

The trajectory component of the refractive ray P_2P_3 in the xy plane is $P_2^{xy}P_3^{xy}$, the slope of the normal line at P_2^{xy} is $k_2' = y_2/(x_2 - a_2 - R_2)$, the incident and refractive angles on the 2nd spherical surface are

$$\theta_2 = \arctan\left|\frac{k_1 - k_2'}{1 + k_1 k_2'}\right|$$
$$\theta_2' = \arcsin(\sin\theta_2 / n(z,t))$$

respectively. The $P_2^{xy}P_3^{xy}$ satisfies the linear ray equation $y = k_2(x - x_2) + y_2$, where the slope k_2 of $P_2^{xy}P_3^{xy}$ is

$$k_2 = \left|\frac{k_2' - \tan\theta_2'}{k_2'\tan\theta_2' + 1}\right|.$$

Therefore, the coordinates of $P_3^{xy}(x_3, y_3)$ can be calculated by the linear ray equation $y = k_2(x - x_2) + y_2$ and the 3rd spherical surface equation $(x - a_3 + R_3)^2 + y^2 = R_3^2$.

To express the ray equation on the $\overline{P_2^{xy}P_3^{xy}}z$ plane, the dynamic coordinate system $x'z$ is established as shown in Fig. 1(d). In the $x'z$ coordinate system, the coordinates of P_2 are $x' = x_2' = 0$ and $z = z_2$, and the line $P_2^{xy}P_3^{xy}$ determines the x' axis. The path infinitesimal element of a ray propagating in the $x'z$ plane satisfies the geometric relationship as shown in Fig. 1(d)

$$(\mathrm{d}s)^2 = (\mathrm{d}z)^2 + (\mathrm{d}x')^2. \tag{1}$$

Let γ_2 and γ_2' be the incident and refractive angles of the ray along the z axis on the 2nd spherical surface, respectively, and according to the invariant form of the Snell law in inhomogeneous media, $n_0 \sin\gamma_2 = n(z,t)\sin\gamma_2'$.[14] Based on the geometric relationship $\mathrm{d}s/\mathrm{d}x' = 1/\sin\gamma$ as shown in Fig. 1(d), the nonlinear ray equation in the liquid core is deduced in the form of 2nd-order differential equation as

$$\frac{\mathrm{d}^2 z}{\mathrm{d}x'^2} = \frac{1}{2n_0^2\sin^2\gamma}\frac{\mathrm{d}(n^2(z,t))}{\mathrm{d}z}, \tag{2}$$

where the incident angle on the 2nd spherical surface is $\gamma = \gamma_2 = 90^\circ$, $\sin\gamma_2 = 1$, equation (1) becomes

$$\frac{\mathrm{d}^2 z}{\mathrm{d}x'^2} = \frac{1}{2n_0^2}\frac{\mathrm{d}(n(z,t)^2)}{\mathrm{d}z} = \frac{n(z,t)}{n_0^2}\frac{\mathrm{d}n(z,t)}{\mathrm{d}z}. \tag{3}$$

Equation (3) has no analytic solution in general, but its numerical solution can be calculated on condition that the RI function $n(z,t)$ is known. For example, if the term on the right-hand side of Eq. (3) is equal to the value of $2u$ at $z = z_1$ and $t = t_0$, the nonlinear ray equation gives out a quadratic curve on the $x'z$ plane, which satisfies

$$z(x') = ux'^2 + vx' + w, \tag{4}$$

where u, v, and w are undetermined coefficients. As the ray enters into the xy plane perpendicular to the z axis, $v = 0$ and $w = z_2 = z_1$. The ray equation on the $x'z$ plane is $z(x') = ux'^2 + z_2$ that is, a nonlinear parabola equation. Substituting $x_3' = \sqrt{(x_3 - x_2)^2 + (y_3 - y_2)^2}$ into Eq. (4), $z(x_3') = z_3$. From the complementary angle of the angle between the tangent line of the point x_3' and the z axis, the incident and refractive angles γ_3 and γ_3', are obtained.

3.3. Linear path of P_3P_4

As the ray leaves the liquid core from the 3rd spherical surface, refractive ray P_3P_4 will propagate on the $\overline{P_3^{xy}P_4^{xy}}z$ plane (homogeneous media, $n = n$), and intersect with 4th spherical surface at P_4, as shown in Figs. 1(c) and 1(d). The trajectory component of P_3P_4 in the xy plane is $P_3^{xy}P_4^{xy}$, the slope of the normal line at P_3^{xy} is $k_3' = y_3/(x_3 - a_3 + R_3)$, the incident and refractive angles on the 3rd spherical surface are

$$\theta_3 = \arctan\left|\frac{k_2 - k_3'}{1 + k_2 k_3'}\right|,$$
$$\theta_3' = \arcsin(n(z,t)\sin\theta_3 / n_0),$$

respectively. The $P_3^{xy}P_4^{xy}$ satisfies the linear ray equation $y = k_3(x - x_3) + y_3$, where the slope of $P_3^{xy}P_4^{xy}$ is

$$k_3 = \left|\frac{k_3' - \tan\theta_3'}{k_3'\tan\theta_3' + 1}\right|.$$

Therefore, the coordinates of $P_4^{xy}(x_4, y_4)$ can be calculated by the linear ray equation $y = k_3(x - x_3) + y_3$ and the 4th spherical surface equation $(x - a_4 + R_4)^2 + y^2 = R_4^2$.

To express the ray equation on the $\overline{P_3^{xy}P_4^{xy}}z$ plane, the dynamic coordinate system $x'z$ is established on the $\overline{P_3^{xy}P_4^{xy}}z$ plane as shown in Fig. 1(d). In the $x'z$ coordinate system, the coordinates of P_3 are $x' = x_3' = 0$ and $z = z_3$, and the line $P_3^{xy}P_4^{xy}$ determines the x' axis. The ray equation of P_3P_4 is $z(x') = k_z x' + z_3$, where $k_z = -\tan\gamma_3'$. Substituting $x_4' = \sqrt{(x_4 - x_3)^2 + (y_4 - y_3)^2}$ into $z(x')$, $z(x_4') = z_4$. The refractive angle γ_4' can be calculated by the incident angle $\gamma_4 = \gamma_3'$ and refraction law.

3.4. Linear path of P_4P_5

After the ray leaves the 4th refractive spherical surface, refractive ray P_4P_5 will propagate on the $\overline{P_4^{xy}P_5^{xy}}z$ plane (homogeneous media, $n = 1$), and intersect with CMOS detection at P_5 as shown in Figs. 1(c) and 1(d). The trajectory component of the refractive ray P_4P_5 in the xy plane is $P_4^{xy}P_5^{xy}$. The slope of the normal line at P_4^{xy} is $k_4' = y_4/(x_4 - a_4 + R_4)$. The incident and refractive angles on the 4th spherical surface are $\theta_4 = \arctan\left|\frac{k_3 - k_4'}{1 + k_3 k_4'}\right|$ and $\theta_4' = \arcsin(n_0\sin\theta_4)$, respectively.

The $P_4^{xy}P_5^{xy}$ satisfies the linear ray equation $y = k_4(x - x_4) + y_4$, where the slope k_4 of $P_4^{xy}P_5^{xy}$ is

$$k_4 = \left| \frac{k_4' - \tan\theta_4'}{k_4' \tan\theta_4' + 1} \right|.$$

Therefore, the coordinates of $P_5^{xy}(x_5, y_5)$ can be calculated by the linear ray equation $y = k_4(x - x_4) + y_4$ and CMOS plane $x = x_5$.

Like P_3P_4, the linear ray equation of P_4P_5 in $x'z$ coordinate system is $z(x') = k_z x' + z_4$, where $k_z = -\tan\gamma_4'$, $z(x_5') = z_5$ is given by $x_5' = \sqrt{(x_5 - x_4)^2 + (y_5 - y_4)^2}$. Hence, the coordinates of $P_5(x_5, y_5, z_5)$ on the CMOS plane are finally determined by the ray tracing method from the ray at incident point $P_1(x_1, y_1, z_1)$.

4. Simulation of diffusion image (1): determining experimental conditions

4.1. Special solution of diffusion equation in dilute solution

In ray tracing calculation, it is necessary to predetermine the spatial and temporal RI profile of diffusion solution in the liquid core. To do so, the one-dimensional diffusion process shown in Figs. 1(a) and 1(b) is assumed to satisfy Fick second law and initial and boundary conditions,[13] which are expressed by Eqs. (5) and (6), respectively,

$$\frac{\partial C(z,t)}{\partial t} = \frac{\partial}{\partial z}\left[D(C) \frac{\partial C(z,t)}{\partial z} \right], \tag{5}$$

$$\begin{cases} C(z > 0,\ t = 0) = C_1, \\ C(z \le 0,\ t = 0) = C_2, \end{cases} \quad \begin{cases} C(z = H,\ t > 0) = C_1, \\ C(z = -H,\ t > 0) = C_2. \end{cases} \tag{6}$$

Here $C(z,t)$ is the concentration space–time profile of the diffusion solution, C_1 and C_2 are the initial concentrations, respectively, on each side of the diffusion interface ($z = 0$). In general, the diffusion coefficient is a function of the concentration, $D = D(C)$, and equation (5) has no analytic solution. On the condition of infinite dilute, the diffusion coefficient is independent of the concentration, $D(C) = D$, and equation (5) has an analytic solution in the form of the Gaussian error function:[25]

$$C(z,t) = \frac{C_1 + C_2}{2} + \frac{C_1 - C_2}{2} \mathrm{erf}\left(\frac{z}{2\sqrt{D_0 t}} \right). \tag{7}$$

Taking for example the diffusion process of TG aqueous solution at room temperature ($T = 298$ K), $D = 0.730 \times 10^{-5}$ cm^2/s can be known by analyzing an instantaneous diffusion image.[1] The RIs of TG aqueous solutions with different concentrations are measured by an abbe refractometer, and the relationship between RI and solution concentration is $n(C) = 0.1251C + 1.3328$ with a linear correlation coefficient of 0.999. The unit of C is mass fraction, $C = 1$ and 0 refer to pure TG and water, respectively. Substituting D and $n(C)$ into Eq. (7), the RI space–time profile $n^s(z,t)$ is obtained.

4.2. Comparison between simulation images in "homogeneous" and "inhomogeneous" media

For better understanding the influence of initial conditions and diffusion time on diffusion image, as collimated beams pass an LCL through "homogeneous" (ignoring ray deviation from entrance plane) or inhomogeneous solution, the diffusion images on the focal plane of the LCL are simulated based on the obtained $n^s(z,t)$ and the ray tracing algorithms described in Section 3.

When the initial concentration difference is $C_2 - C_1 = 1.0$ (100%), the simulated results are shown in the upper part of Fig. 2, indicating that there are significant differences both in image contour and in focus position as shown in Figs. 2(a)–2(c) and Figs. 2(a′)–2(c′), existing between "homogeneous" or inhomogeneous solutions. However, the differences decrease gradually with the diffusion time going by. The relative deviations of concentration between the images calculated in "homogeneous" and inhomogeneous solutions show further that the maximum value of deviation is 49.7% at $t = 20$ min in Fig. 2(a″), which decreases to 10.2 % at $t = 270$ min in Fig. 2(c″).

When the initial concentration difference decreases to $C_2 - C_1 = 0.6$ (60%), two kinds of diffusion images are also calculated under the conditions of "homogeneous" and inhomogeneous solutions, and their results are shown in the lower part of Fig. 2. Compared with the results of $C_2 - C_1 = 1.0$ (100%), the differences in image contour and focus position obviously decrease as shown in Figs. 2(d)–2(f) and Figs. 2(d′)–2(f′). The maximum value of relative deviation is 26.6% at $t = 20$ min in Fig. 2(d″), which decreases sharply to 2.1 % at $t = 270$ min in Fig. 2(f″).

The simulation results shown in Fig. 2 demonstrate that either reducing the initial concentration difference or increasing the diffusion time can obviously lessen RI gradient of diffusion solution, and then make the two kinds of simulated images more closer. In the case of TG aqueous solution diffusion, the relative deviation of concentration between the two simulations will be less than 2.1% as $C_2 - C_1$ and diffusion time are set to be 0.6 and larger than 270 min, respectively. Under the premise of meeting the above conditions, it is reasonable to treat the light beam as passing through "homogeneous" solution, and the light beam deviation from entrance plane is ignorable.

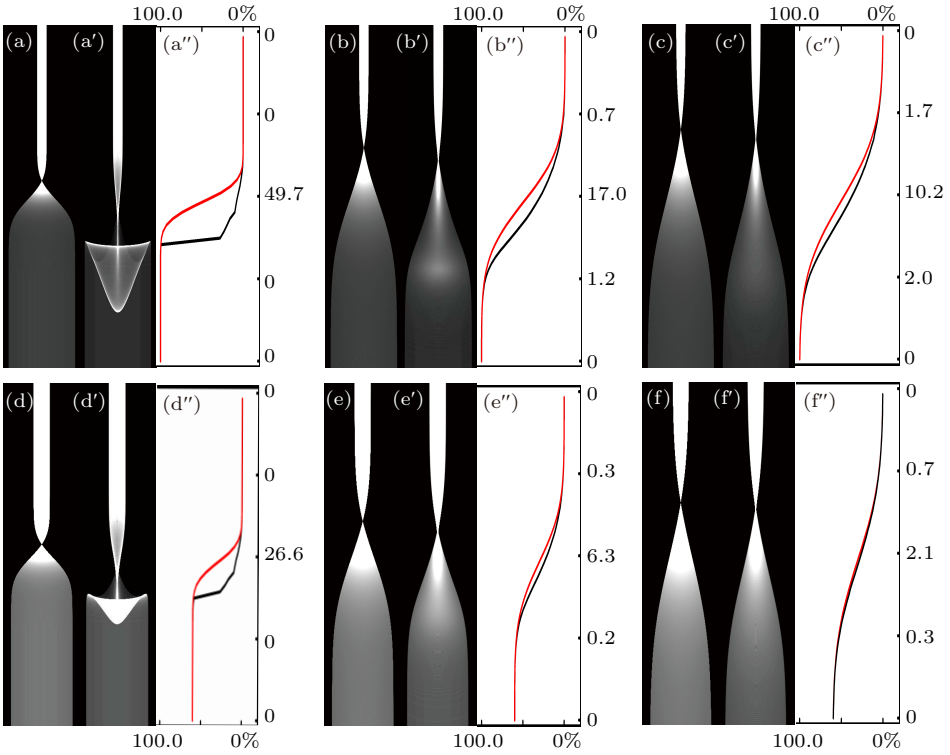


Fig. 2. Comparison between two simulated results. (a)–(f): Simulated diffusion images in "homogeneous media", where (a), (b), (c): $C_2 - C_1 = 1.0$, $t = 20$, 150, 270 min; (d), (e), (f): $C_2 - C_1 = 0.6$, $t = 20$, 150, 270 min; (a′)–(f′): simulated diffusion images in inhomogeneous media; (a″)–(f″) the concentration relative deviations of two kinds of simulations.

5. Diffusion experiments and spatial and temporal concentration profile of TG solution

Based on the analysis in Section 4, under the conditions of initial concentration difference $C_2 - C_1 = 0.6$ and room temperature (298 K), two groups of diffusion experiments of TG aqueous solution are carried out to combine a complete concentration range from $C = 0$ to 1, the $C_1 = 0$, $C_2 = 0.6$ (0%–60%) and $C_1 = 0.4$, $C_2 = 1.0$ (40%–100%) for the first and second groups, respectively. Taking the first group for example, a digital injection pump is used to inject 60% TG aqueous solution ($C_2 = 0.6$) into the lower half of the LCL ($H = 25$ mm). Waiting for 10 min to reduce liquid turbulence interference, distilled water ($C_1 = 0$) is slowly injected into the upper half of the LCL at a speed of 2.0 ml/min ($H = 25$ mm), ensuring that there is no significant convection interference between the two liquids. The time when the two liquids contact each other is set to be the initial diffusion time ($t = 0$). The CMOS detector is fixed at the position where the collimated beam can be sharply imaged in the liquid thin layer with RI $(n) = n_c = 1.3482$, and images are collected in the interval of 2 min. The experimental operation for the second experimental group is similar to that for the first group, but the CMOS detector is fixed at the position where the collimated beams could be sharply imaged in the liquid thin layer with RI $(n) = n_c = 1.3994$.

To simultaneously satisfy the diffusion time required by the above simulated calculation and the initial conditions in Eq. (6), diffusion images during 306 min–380 min and 450 min–540 min are selected to calculate the concentration-dependent diffusion coefficients $D(C)$ for the first and second diffusion group, respectively.

The typical diffusion images are shown in Fig. 3, where figures 3(a) and 3(b) show the diffusion images of the first group at $t_0 = 320$ min and 380 min. Figures 3(c) and 3(d) show the diffusion images of the second group at $t_0 = 450$ min and 540 min. After the processing of the binarization digital image, the extraction of the image width, and the transformation of the image width and the solution concentration, a series of experimental concentration spatial and temporal profiles $C^e(z_j, t)$s are achieved. Some of curves corresponding to those in Fig. 3 are plotted by the rectangular points as shown in Fig. 4.

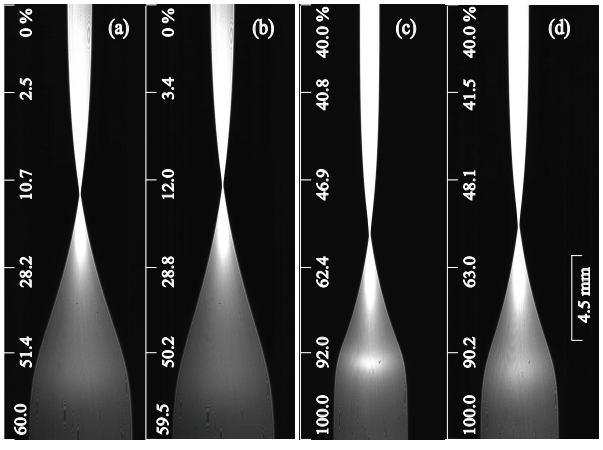


Fig. 3. Typical experimental diffusion images for [(a) and (b)] 0%–60% diffusion group at $t = 320$ min (a) and 380 min (b), and [(c) and (d)] 40%–10% diffusion group at $t = 450$ min (c) and 540 min (d).

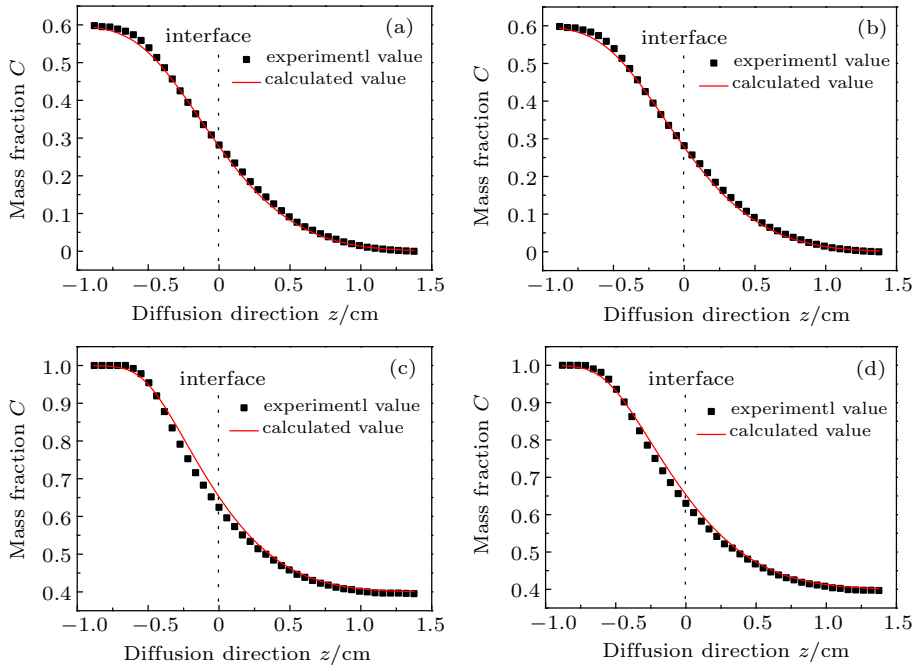


Fig. 4. Spatial and temporal concentration profiles $C^{\mathrm{e}}(z_j,t)$s corresponding to Fig. 3, at $t=320$ min (a), 380 min (b), 450 min (c), and 540 min (d), with rectangular points representing experimental values, and solid red lines denoting calculated values.

6. Numerical solution of diffusion equation and determination of $D(C)$

In general, the diffusion coefficient is dependent on concentration and written as $D(C)$. The $D(C)$ can be expressed in the form of polynomial as

$$D(C)=D_0(1+\alpha_1 C+\alpha_2 C^2+\alpha_3 C^3\cdots), \tag{8}$$

where α_1, α_2, α_3, ... are the undetermined coefficients, D is the constant diffusion coefficient obtained by instantaneous image analytical method under the infinite dilute condition,[24] equation (5) can be expanded as

$$\frac{\partial C(z,t)}{\partial t}=\frac{\partial D(C)}{\partial z}\frac{\partial C(z,t)}{\partial z}+D(C)\frac{\partial^2 C(z,t)}{\partial z^2}. \tag{9}$$

Partial differential equation (9) has no analytic solution on condition that the $D(C)$ is undetermined. The algorithm of FDM is used to calculate the numerical solution of Eq. (9) in this paper. The spatial distance is divided into discrete $M+2$ terms, $j=0$ and $M+1$ are the boundary terms. Equations (9) and (6) are changed into the difference quotient form, respectively,

$$\begin{aligned}&\left(\frac{r^i_{j+1}-r^i_{j-1}}{4}-r^i_j\right)C^{i+1}_{j-1}+(1+2r^i_j)C^{i+1}_j\\&+\left(-\frac{r^i_{j+1}-r^i_{j-1}}{4}-r^i_j\right)C^{i+1}_{j+1}=C^i_j,\\&(z=jh, j=0,1,2,\ldots,M+1),\end{aligned} \tag{10}$$

$$\begin{cases} i=0\ \ (t=0),\\ j>M/2+1,\ \ C^{i=0}_j=C_1,\\ j\le M/2+1,\ \ C^{i=0}_j=C_2,\end{cases}\quad \begin{cases}\infty>i>0\ \ (t>0),\\ j=M+1,\ \ C^i_{M+1}=C_1,\ \ D^i_{M+1}=D_0,\\ j=0,\ \ C^i_0=C_2,\\ j<M+1,\ \ D^i_j=D_0\times\left[1+\alpha_1 C^i_j+\alpha_2\left(C^i_j\right)^2+\alpha_3\left(C^i_j\right)^3+\cdots\right],\end{cases} \tag{11}$$

where, $r^i_{j-1}=(\tau\times D^i_{j-1})/h^2$, $r^i_j=(\tau\times D^i_j)/h^2$, $r^i_{j+1}=(\tau\times D^i_{j+1})/h^2$.

Equation (10) is further expanded into M linear equations along the diffusion direction ($z=jh, j=0,1,2,\ldots,M+1$). By varying under-determined parameters $[(\alpha_1)_k, (\alpha_2)_k, (\alpha_3)_k]$, a series of calculating $C^n(z_j,t_i)$s of Eq. (10) at a special moment $t_i=t$ is used to compare with the experimental profile $C^{\mathrm{e}}(z_j,t_0)$, and standard deviation σ_k is calculated. The minimum value of σ_k is the best-fit parameters of TG at $t_i=t_0$, the corresponding concentration values calculated are shown in Fig. 4 by the solid lines. $C^n_{\mathrm{fit}}(z_j,t_0)$ and $C^{\mathrm{e}}(z_j,t_0)$ are in good agreement in the whole concentration area, which indicates that the $D(C)$ relation calculated by comparing the experimental curve is reliable.

For the first diffusion experimental group, 10 diffusion images acquired in the interval of 5 min during the period from

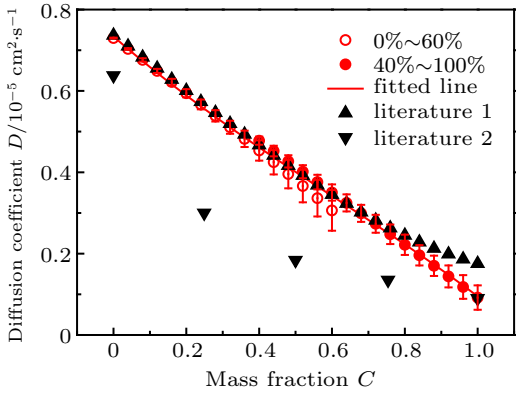


Fig. 5. Comparison of $D(C)$ between measured values and literature values. Red empty circle represents measured value of $D_1(C)$ in concentration range of 0%–60%. Solid red circle denotes measured value of $D_2(C)$ in concentration range of 40%–100%. Solid line refers to fitting curve $D(C)$ in concentration range of 0%–100%. Upper triangle represents measured values of literature 1. Lower triangles are for measured values of literature 2. Error bars, which are magnified 5 times for the sake of clarity, are determined by ten-time independent measurements.

305 min to 350 min, are used to calculate $D(C)$ relations, the average values are listed in Table 1, which satisfy $D_1(C) = 0.730\times10^{-5}(1-0.916C-0.058C^2-0.045C^3)$ cm^2/s in the concentration range from $C=0.0$ to 0.6, and $D_1(C)$ *versus* mass fraction C is shown in Fig. 5 by the red empty circles. For the second group, 10 diffusion images acquired in the interval of 10 min during the period from 450 min to 540 min, are used to calculate $D(C)$ relations, the average values are listed in Table 2, which satisfy $D_2(C) = 0.730\times10^{-5}(1-0.860C-0.008C^2-0.006C^3)$ cm^2/s in the concentration range from $C=0.4$ to 1.0, and the $D_2(C)$ *versus* mass fraction C is shown in Fig. 5 by the red solid circles.

To simply express the liquid diffusion coefficients $D(C)$ in the whole concentration range by one formula, let the diffusion coefficients be $D_1(C)$ in the range of $C=0$ to 0.4, $D_2(C)$ in the range of $C=0.6$ to 1.0, and average value of $D_1(C)$ and $D_2(C)$ in the range of $C=0.4$ to 0.6, the $D(C)$ relation is refitted by the least square method in the range of $C=0$ to 1, the fitted result is

$$D(C) = 0.7339\times10^{-5} \times(1-1.068C+0.444C^2-0.2465C^3), \quad (12)$$

which is drawn by the red solid line in Fig. 5. For the convenience of comparison, the literature values of Ferna'ndez-Sempere (1996)[22] and Bogachev (1982)[23] for the same diffusion solution and temperature are also shown in Fig. 5, which indicates that the values in the present paper are distributed between the two literature values, and much closer to those measured by Ferna'ndez-Sempere with holographic interferometry.[22]

Table 1. Measurement and calculation results of $D(C)$ in a range of 0%–60% concentration.

	$D(C)/10^{-5}$ cm^2·s^{-1}									
C/MF	0.0	0.1	0.2	0.3	0.4	0.5	0.6	α_1	α_2	α_3
$\overline{D}_{305\ \mathrm{min}-350\ \mathrm{min}}$	0.730	0.663	0.594	0.525	0.454	0.381	0.307	–0.916	–0.058	–0.045
STD	0.00	0.001	0.002	0.003	0.005	0.007	0.010	0.008	0.019	0.022
RSD/%	0.00	0.151	0.337	0.571	1.101	1.837	3.257			
$D_1(C) = 0.730\times10^{-5}(1-0.916C-0.058C^2-0.045C^3)$ cm^2/s										

Table 2. Measurement and calculation results of $D(C)$ in a range of 40%–100% concentration.

	$D(C)/10^{-5}$ cm^2·s^{-1}									
C/MF	0.4	0.5	0.6	0.7	0.8	0.9	1.0	α_1	α_2	α_3
$\overline{D}_{450\ \mathrm{min}-540\ \mathrm{min}}$	0.478	0.414	0.350	0.286	0.222	0.157	0.092	–0.860	–0.008	–0.006
STD	0.002	0.003	0.004	0.004	0.004	0.005	0.006	0.006	0.003	0.003
RSD/%	0.418	0.725	1.143	1.399	1.802	3.185	6.522			
$D_2(C) = 0.730\times10^{-5}(1-0.860C-0.008C^2-0.006C^3)$ cm^2/s										

7. Simulation of diffusion image (2) for verifying correctness of measurement results

It is worth noting that equation (12) is reliable in the whole diffusion process, though it is obtained by using the images acquired during the diffusion time from 305 min to 540 min. A prominent advantage of measuring $D(C)$ relation introduced in the paper is that the correctness of deduced $D(C)$ can be verified by comparing simulated images with experimental images in the whole diffusion process.

The algorithm of FDM is used to directly solve the diffusion Eq. (5) under the conditions of Eq. (11) and deduced $D(C)$, and obtain the numerical solution of spatial and temporal concentration profiles $C^n(z_jt_i)$ $(j=0,1,\ldots,M+1;\ i=0,1,2,\ldots)$. The $C^n(z_jt_i)$ are then converted into spatial and temporal RI profiles $n(z_jt_i)$ $(j=0,1,\ldots,M+1;\ i=0,1,2,\ldots)$ by means of experimental relationship of $n(C)=0.1251C+1.3328$. The undetermined coefficient u in nonlinear optical Eq. (4) satisfies the difference form

$$2u_j^i = \frac{n_j^i}{n_0^2}\frac{n_{j+1}^i-n_j^i}{h} = \left[0.0068C_j^i+0.0725\right]\frac{C_{j+1}^i-C_j^i}{h}. \quad (13)$$

Based on the ray equations derived in Section 3 and the $n(z_j,t_i)$, the ray tracing method is again used to calculate the images at any diffusion time and any imaging position where different liquid thin layers of RI can be sharply imaged. The simulated images are compared with the experimental images at the same conditions, which are shown in Figs. 6 and 7.

When the virtual CMOS detector is placed at the position where the thin layer of RI $= n = 1.3482$ can be sharply imaged, the experimental diffusion images for the first group at $t = t_0 = 25$, 210, and 380 min are shown in Figs. 6(a′)–6(c′). The two kinds of simulated diffusion images are also shown in Fig. 6 for the convenience of comparison, where figures 6(a)–6(c) are the images ignoring the ray deviation from entrance plane and figures 6(a″)–6(c″) are the images that the ray deviation is calculated strictly when light ray passes through the inhomogeneous solution in the used LCL.

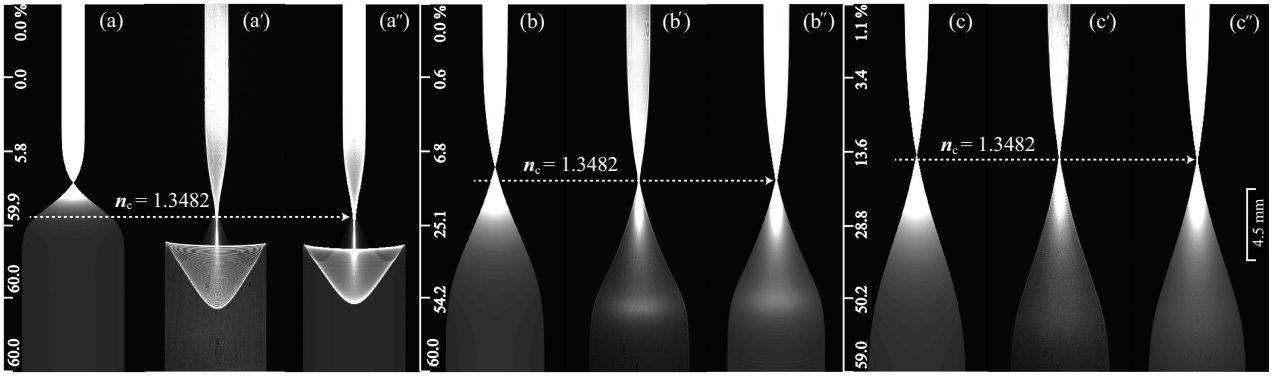


Fig. 6. Comparison between experimental diffusion images and simulated images at RI $= n_c = 1.3482$ for the first diffusion group (0%–60%): [(a′), (b′), (c′)] experimental diffusion images at $t = 25$, 210, and 380 min; [(a), (b), (c)] simulated images in "homogeneous solution"; [(a″, b″, c″)]: simulated images in inhomogeneous solution. Longitudinal scales represent solution concentrations.

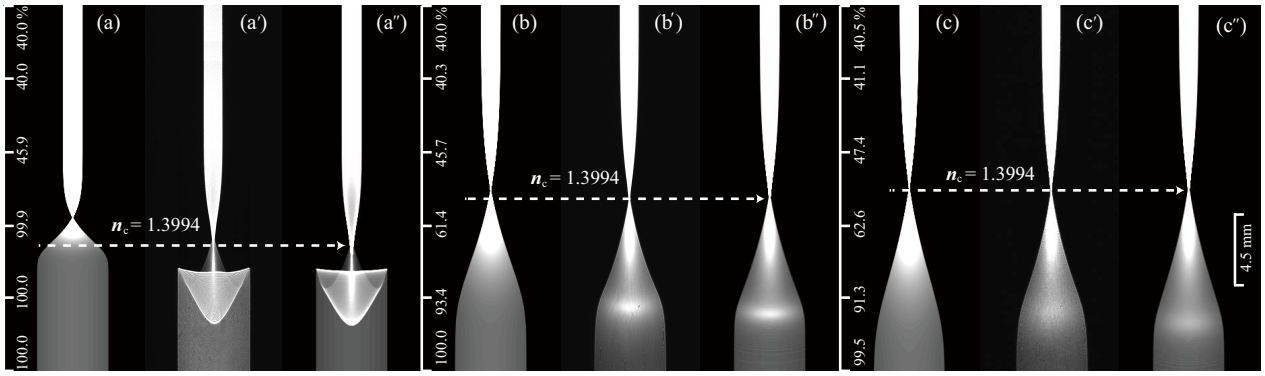


Fig. 7. Comparison between experimental diffusion images and simulated images at RI $= n_c = 1.3994$ for the second diffusion group (40%–100%): [(a′), (b′), (c′)] experimental diffusion images at $t = 40$, 360, and 540 min; [(a), (b), (c)] simulated images in "homogeneous solution"; [(a″), (b″), (c″)] simulated images in inhomogeneous solution. Longitudinal scales represent solution concentrations.

The comparison of the experimental diffusion images with two kinds of simulated diffusion images clearly shows some points as follows. (i) Under strict simulation conditions, the simulated diffusion images shown in Figs. 6(a″)–6(c″) are in very good agreement with the experimental images shown in Figs. 6(a′)–6(c′) in a wide diffusion time range from $t = 25$ min to 380 min, whether on the image contours, focal positions, or intensity distributions. (ii) Ignoring the ray deviation from entrance plane, only at the later stage of the diffusion process ($t = 380$ min), does the simulated diffusion image figure 6(c) coincide with the experimental diffusion image (Fig. 6(c′)).

As the virtual CMOS detector is placed at the position where the thin layer of RI $= n = 1.3994$ can be sharply imaged, the experimental diffusion images for the second group at $t = t = 40$, 360, and 540 min are shown in Figs. 7(a′)–7(c′). The two kinds of simulated diffusion images are also shown in Fig. 7 for the convenience of comparison, where figures 7(a)–7(c) show the images ignoring the ray deviation from entrance plane. Figures 7(a″)–7(c″) show the images that the ray deviation is calculated strictly when ray passes through the inhomogeneous solution in the used LCL.

The same phenomena appearing in Fig. 6 are also found in Fig. 7, implying that the location of virtual CMOS detector does not affect the simulation calculation of diffusion image. In addition, it is interesting to note that the focal positions of the experimental diffusion images, marked by the dotted line arrows both in Figs. 6 and 7 drift slowly upward with the diffusion time going by. This macroscopic image movement is caused by microscopic molecular thermal movement, and the

simulated diffusion images reflect faithfully the law of thermal movement.

Furthermore, as the location of virtual CMOS detector moves to the position where the layer of $n_c = 1.3398$ is sharply imaged, the whole dynamic diffusion process is simulated and compared with the experimental diffusion process. The comparison between two diffusion processes is shown in visualization 1, which not only provides a vivid observation of the dynamic diffusion process, but also shows a solid verification of deduced $D(C)$ due to the high consistency between the experimental process and the simulated process.

8. Conclusions

Ray equations in an LCL are established by using the ray tracing method, and the diffusion images on the focal plane of the LCL are simulated numerically, showing that the ray propagation law in homogeneous media can be used to calculate approximately the diffusion images in inhomogeneous media under the condition of small RI gradient of diffusion the solution. Based on the calculated conditions, the liquid diffusion process of TG aqueous solution in the LCL is experimentally implemented at room temperature, thus obtaining the liquid diffusion coefficient of TG aqueous solution $D(C)$, which is dependent on the solution concentration. The spatial and temporal concentration profile $C^e(z,t)$ is acquired by selecting the experimental diffusion images at the late stage of the diffusion process. The $D(C)$ is expressed in the form of polynomial with a series of underdetermined parameters. The FDM method is used to calculate the spatial and temporal concentration profiles $C^n(z,t)$ of diffusion solution by varying the underdetermined parameters, and $D(C) = 0.730 \times 10^{-5}(1 - 1.068C + 0.444C^2 - 0.2465C^3)$ cm^2/s is obtained by comparing the $C^e(z,t)$ and $C^n(z,t)$. Based on the ray equations and the RI spatial and temporal profiles $n(z,t)$ in the whole diffusion process calculated by the obtained $D(C)$, we simulate strictly the diffusion images in an inhomogeneous solution. The simulated results are highly consistent with the experimental images in image contour, focal position, and light intensity distribution, which verifies not only the correctness of $D(C)$ measurement result, but also the reliability of studying ray propagation in the LCL composed of inhomogeneous diffusion solution.

References

[1] Meng W D, Xia Y, Song F X and Pu X Y 2017 *Opt. Express* **25** 5626
[2] Sun L C, Du C, Li Q and Pu X Y 2016 *Appl. Opt.* **55** 2011
[3] Kim B, Yang J, Lee D, Choi B, Hyeon T and Park J 2018 *Adv. Mater.* **30** 1703316
[4] Cussler E L 2009 *Diffusion: Mass Transfer in Fluid Systems*, 3nd edn. (New York: Cambridge University Press) pp. 126–134
[5] Zhang J X 2018 *Appl. Therm. Eng.* **129** 564
[6] Ali H, Zhang D, Wagner J and Park C 2018 *Energies* **11** 899
[7] Ju Y Y, Zhang Q M, Gong Z Z and Ji G F 2013 *Chin. Phys. B* **22** 083101
[8] Li Q and Pu X Y 2013 *Acta Phys. Sin.* **62** 094206 (in Chinese)
[9] Wolff L, Zangi P, Brands T, Rausch M H, Koß H J, Fröoba A P and Bardow A 2018 *Int. J. Thermophys.* **39** 133
[10] Siebel D, Scharfer P and Schabel W 2015 *Macromolecules* **48** 8608
[11] Leonhardt U 2009 *New. J. Phys.* **11** 093
[12] Moore D T 1980 *Appl. Opt.* **19** 1035
[13] Crank J 1975 *The Mathematics of Diffusion*, 2nd edn. (London: Oxford University Press) pp. 104–137
[14] Zhong X H 2003 *Modern fundamentals of optics* (Beijing: Peking University Press) pp. 22–25
[15] Zhao J M, Tan J Y and Liu L H 2015 *J. Quantum Spectrosc. Rad.* **152** 114
[16] Wu C Y and Hou M F 2012 *Int. J. Heat. Mass. Transfer* **55** 6600
[17] Luneburg R K and Herzberger M 1964 *Mathematical theory of optics* (Berkeley: University of California Press) pp. 100–125
[18] Navarro R and Moreno-Barriuso E 1999 *Opt. Lett.* **24** 951
[19] Schurig D, Pendry J B and Smith D R 2006 *Opt. Express* **14** 9794
[20] Taflove A and Hagness S C 2005 *Computational electrodynamics: the finite-difference time-domain method*, 3nd edn. (Boston: Artech House) pp. 35–50
[21] Murio D A 2008 *Comput. Math. Appl.* **56** 1138
[22] Fernández-Sempere J, Ruiz-Beviá F, Colom-Valiente J and Más-Pérez F 1996 *J. Chem. Eng. Data* **41** 47
[23] Bogacheva I S, Zemdikhanov K B and Usmanov A G 1982 *Izv. Vyssh. Uchebn. Zaved., Khim. Khim. Tekhnol.* **25** 182
[24] Sun L C, Meng W D and Pu X Y 2015 *Opt. Express* **23** 23155
[25] Rashidnia N and Balasubramaniam R 2002 *Appl. Opt.* **41** 1337